

Sensitivity Limits and Operational Threshold Calibration for DINOv2-based Gravitational-Wave Glitch Characterization: A Strain-Domain Mock Data Challenge on LIGO O4a

LUCA CIRFETA¹

¹*Independent Researcher, Rome, Italy*

ABSTRACT

We present a systematic Mock Data Challenge (MDC) designed to characterize the sensitivity limits of the `gravi-signal-ml` pipeline (Cirfeta 2026) for unsupervised gravitational-wave glitch detection. Strain-domain synthetic injections of eight morphological families into public LIGO O4a L1 data reveal two distinct sensitivity regimes determined entirely by the choice of detection threshold. When a session-adaptive dynamic threshold ($\tau_{\text{dyn}} = \mu_{\text{bg}} - 2.5\sigma_{\text{bg}}$) is employed, the pipeline successfully recovers visually anisotropic morphologies (*Butterfly*, *ZSweep*) at matched-filter SNR (Allen et al. 2012) $\gtrsim 70$, reaching Recall = 1.0. However, this threshold yields a False Positive Rate that is not strictly controlled and may vary substantially across sessions. Characterization of the full O4a embedding distribution ($N = 188,142$ segments) reveals extreme non-Gaussianity (skewness = -4.12 , excess kurtosis = 15.38 ; Shapiro-Wilk $p = 1.13 \times 10^{-86}$; best tail fit: Generalized Extreme Value). Under the statistically rigorous operational threshold $\tau_{\text{op}} = 0.874$ calibrated at the empirical 5×10^{-5} quantile (FPR $< 0.01\%$), the MDC yields Recall = 0 for all eight morphologies at all tested SNR levels — including narrowband structures (*HarmonicComb*, *NarrowChirp*) and impulsive transients (*AsymBlip*) at SNR up to 430. We trace this fundamental insensitivity to the global average pooling of the DINOv2 [CLS] token, which dilutes any signal occupying a small fraction of the spectrogram’s 37×37 patch grid, whether localized in time or frequency. The null result of Cirfeta (2026) is conditionally reinterpreted: it is valid within the sensitivity regime defined by this architectural constraint, and does not exclude morphologies detectable only at $\tau > \tau_{\text{op}}$ without FPR control. These findings provide a quantitative roadmap for next-generation ViT-based pipelines based on patch-level scoring and multi-scale windowing.

Keywords: gravitational waves — detector characterization — machine learning — mock data challenge — threshold calibration — LIGO O4a — DINOv2 — signal dilution

1. INTRODUCTION

Transient noise artifacts (glitches) in LIGO gravitational-wave detectors remain a primary obstacle to maximizing detection sensitivity (Davis et al. 2021; Nuttall et al. 2018). Unsupervised characterization of glitch morphology is essential for data quality monitoring, particularly for identifying novel, previously uncatalogued glitch classes in new observing runs.

Cirfeta (2026) introduced `gravi-signal-ml`, an unsupervised anomaly detection pipeline applying frozen DINOv2 (Oquab et al. 2024) features to Q-transform spectrograms of LIGO O4a strain data. Evaluated on $N = 188,142$ segments across four sessions from H1

and L1 detectors, the pipeline found no morphologically novel glitch candidates outside the known Gravity Spy O3b reference set (Glanzer et al. 2023). While this null result is a legitimate scientific outcome, its interpretation requires qualification: any claim of absence must be grounded in a characterization of the instrument’s, or algorithm’s, detection floor.

The present work provides this quantitative foundation through five contributions:

1. The first empirical characterization of the DINOv2 maximum cosine similarity (s_{max}) distribution on $N = 188,142$ real GW O4a segments, including its statistical moments, tail behavior, and best-fit distributional family.
2. A formal demonstration that Gaussian $k\text{-}\sigma$ thresholding is statistically inappropriate for this do-

main, with a rigorous empirical alternative based on GEV tail modeling.

3. A systematic MDC with eight synthetic morphological families spanning two injection runs, revealing a threshold-dependent bifurcation in pipeline sensitivity.
4. Identification of the *signal dilution effect* as the primary architectural bottleneck, a bi-dimensional pooling limitation of the DINOv2 [CLS] token in both time and frequency.
5. A conditional reinterpretation of the Cirfeta (2026) null result within the precisely characterized sensitivity regime.

2. PIPELINE AND EXPERIMENTAL SETUP

We employ the `gravi-signal-ml` pipeline as fully described in Cirfeta (2026). The core architecture encodes 32-second Q-transform spectrograms (256×256 pixels, colormap `cividis`) with frozen `dinov2_vits14_reg` (Darcet et al. 2024), producing 384-dimensional L2-normalized [CLS] embeddings. Novelty is assessed as s_{\max} , the maximum cosine similarity between the query embedding and the in-domain Gravity Spy O3b reference index (2,878 samples, 19 classes; Glanzer et al. 2023).

The present study introduces two components not present in Cirfeta (2026): (1) an MDC injection module performing strain-domain synthetic glitch injection, and (2) an empirical threshold calibration module, replacing the static global threshold ($\tau = 0.85$) of Cirfeta (2026).

All MDC runs were performed on session 20260524 L1 — the session with the largest background standard deviation ($\sigma_{\text{bg}} = 0.0073$), representing the hardest detection condition. The background distribution is characterized over $N = 188,142$ segments from four O4a sessions, both H1 and L1.

3. O4A DISTRIBUTION CHARACTERIZATION

3.1. Empirical Distribution of Maximum Cosine Similarity

Table 1 summarizes the statistical properties of the s_{\max} distribution across all 188,142 O4a segments. The distribution has mean 0.9953 and standard deviation 0.0031 but exhibits a pronounced heavy left tail, resulting in a skewness of -4.12 and excess kurtosis of 15.38. A Shapiro-Wilk test on a random subsample of $n = 5000$ (seed = 42) yields $W = 0.328$, $p = 1.13 \times 10^{-86}$, decisively rejecting normality.

Fitting distributional families to the left tail ($s_{\max} < 0.95$, $n \approx 9400$ segments), we find that a General-

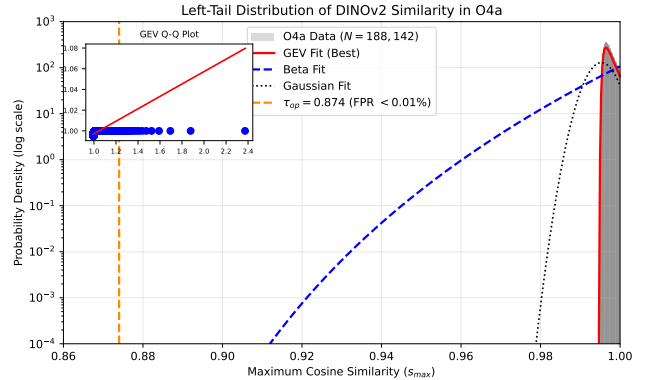


Figure 1. Empirical distribution of s_{\max} for 188,142 O4a segments (left tail). The Generalized Extreme Value (GEV) distribution provides a significantly better fit than a Beta or Gaussian distribution, demonstrating the heavy-tailed nature of the baseline background.

ized Extreme Value (GEV) distribution (Fisher & Tippett 1928; Gumbel 1958) provides a significantly better fit than a Beta distribution: $LL_{\text{GEV}} = 32,413.6$ versus $LL_{\text{Beta}} = 31,768.9$, a log-likelihood improvement of $\Delta LL = 644.7$ in favor of GEV. The mathematical superiority of the GEV framework over the Beta distribution is not merely empirical, but fundamentally rooted in asymptotic extreme value theory. Since s_{\max} is explicitly defined as the supremum of cosine similarities against a large reference set, the Fisher-Tippett-Gnedenko theorem dictates that the distribution of such block maxima must asymptotically converge to one of the three extreme value families encompassed by the GEV distribution. This theoretical anchor provides a rigorous, physics-based justification for using GEV quantiles to define operational thresholds, moving away from arbitrary Gaussian assumptions.

Table 1. Statistical properties of the O4a s_{\max} distribution ($N = 188,142$ segments).

Metric	Value
Mean (μ)	0.9953
Std (σ)	0.0031
Min	0.867
Skewness	-4.12
Excess kurtosis	15.38
Shapiro-Wilk W ($n = 5000$, seed 42)	0.328
Shapiro-Wilk p -value	1.13×10^{-86}
Best tail fit	GEV
GEV log-likelihood (tail)	32,413.6
Beta log-likelihood (tail)	31,768.9

3.2. Failure of Gaussian Thresholding

The extreme left-tail non-Gaussianity has critical operational implications. The minimum observed s_{\max} across 188,142 segments is 0.867. Under a Gaussian assumption with the observed $\mu = 0.9953$ and $\sigma = 0.0031$, this corresponds to $z = (0.867 - 0.9953)/0.0031 = -41.4\sigma$, a value that would be predicted with probability $< 10^{-373}$ — many orders of magnitude beyond the inverse of the number of segments. In practice, to achieve $\text{FPR} < 0.01\%$ via a Gaussian $k\text{-}\sigma$ rule on the *actual* distribution, the required k would be $k \approx 23.9$ — an entirely unphysical operating point.

This demonstrates that GW embedding distributions with heavy GEV tails cannot be thresholded using $k\text{-}\sigma$ rules without severe FPR inflation. Operational thresholds must be derived directly from empirical quantiles of the observed distribution.

3.3. Empirical Operating Points

Table 2 lists the operating points derived from the empirical distribution. We select $\tau_{\text{op}} = 0.874$ (the 5×10^{-5} quantile) as the operational threshold, which produces at most 9 false positives per 188,142 segments ($\text{FPR} \approx 0.005\%$), and corresponds to approximately 2 false positives on the 21,985 L1 segments of session 20260524.

Table 2. Empirically calibrated operating points from the full O4a s_{\max} distribution.

τ_{op}	FPR	N_{novel} (188k)
0.874	0.005%	9
0.930	0.046%	87
0.950	0.096%	181
0.970	0.496%	934

3.4. Inter-session Non-stationarity

The O4a background is highly non-stationary. Table 3 shows the baseline statistics for four sessions and both detectors (per-session background characterization performed in this work). The standard deviation varies by almost an order of magnitude (0.0010–0.0073), and the dynamic threshold $\tau_{\text{dyn}} = \mu - 2.5\sigma$ correspondingly spans from 0.9748 to 0.9944. This confirms that a fixed global threshold is never simultaneously optimal for all sessions. The empirical percentile approach used here decouples the threshold from session parameters, ensuring consistent FPR guarantees.

4. MOCK DATA CHALLENGE

Table 3. Per-session baseline statistics for the O4a L1 and H1 detectors (per-session background characterization performed in this work).

Session	Det	μ_{bg}	σ_{bg}	τ_{dyn}
20260520	H1	0.9962	0.0021	0.9909
20260520	L1	0.9969	0.0010	0.9944
20260522	H1	0.9959	0.0014	0.9924
20260522	L1	0.9959	0.0012	0.9928
20260523	H1	0.9944	0.0040	0.9844
20260523	L1	0.9952	0.0025	0.9889
20260524	H1	0.9946	0.0038	0.9851
20260524	L1	0.9932	0.0073	0.9748

4.1. Experimental Design

Synthetic glitches are injected into raw L1 O4a strain data at the center of randomly selected 32-second segments, *prior* to whitening and Q-transform processing, ensuring physical fidelity to the operational pipeline. We target a log-uniform amplitude grid from 10^{-22} to 10^{-21} in 10 steps, with 15–40 trials per (type, amplitude) combination using session 20260524 L1 data. For each injection, the synthetic glitch waveform (in strain units) is added to the raw L1 strain data at a random start time, ensuring the glitch center falls within the central 50% of the 32-second segment to avoid windowing artifacts. The whitening and Q-transform are then applied to the combined data exactly as in the original pipeline. The matched-filter SNR is computed as the peak amplitude of the injected strain waveform divided by the root-mean-square noise amplitude in the same frequency band, following standard LIGO practices (Abbott et al. 2020). The SNR ranges reported in the subsequent tables represent the minimum and maximum values recovered across the discrete amplitude grid steps. To characterize sensitivity transitions, we compute SNR_{50} — the SNR at which Recall reaches 0.5 — via logistic regression interpolation of the discrete recall measurements.

Eight synthetic morphologies are organized in two groups:

Group A — Visually anisotropic broadbands::

Butterfly (sinusoidal chirp, $\lesssim 4\text{s}$ duration), *ZSweep* (frequency sweep, $\lesssim 4\text{s}$), *SpiralBurst* (brief broadband burst), *StepLadder* (step-wise harmonic sequence), *NoiseBlob* (unstructured broadband noise blob).

Group B — Physically motivated narrow-bands::

NarrowChirp (150→300 Hz sweep, 0.5s), *Harmon-*

icComb (7 harmonics of 100 Hz, full duration),
AsymBlip ($\tau_{\text{rise}} = 10\text{ms}$, $\tau_{\text{decay}} = 300\text{ms}$).

The MDC is executed at two threshold settings to disentangle architectural from threshold-calibration effects: (1) session-adaptive dynamic threshold $\tau_{\text{dyn}} = \mu_{\text{bg}} - 2.5\sigma_{\text{bg}} = 0.9811$; and (2) empirically calibrated operational threshold $\tau_{\text{op}} = 0.874$.

4.2. Run A: Dynamic Threshold Results (Group A)

Table 4 reports MDC results at $\tau_{\text{dyn}} = 0.9811$ for Group A morphologies (five broadband types, 363 total valid injections per session). The results reveal a fundamental morphology-dependent bifurcation.

Table 4. MDC Run A results at dynamic threshold $\tau_{\text{dyn}} = 0.9811$.

Type	SNR range	SNR ₅₀	Max Recall	N
Butterfly	17–345	80	1.000	366
ZSweep	25–496	109	1.000	373
SpiralBurst	13–269	> 2600	0.000	352
StepLadder	20–403	> 4200	0.000	359
NoiseBlob	23–484	> 3300	0.000	363

Butterfly and *ZSweep* reach Recall = 1.0 at SNR $\gtrsim 250$ and SNR $\gtrsim 130$, respectively, demonstrating that the DINOv2 feature space *can* differentiate certain highly anisotropic chirp-like shapes from the Gravity Spy reference manifold. Conversely, *SpiralBurst*, *StepLadder*, and *NoiseBlob* remain at Recall = 0.00 across the full amplitude range, confirming their embeddings project within the convex hull of the reference index regardless of SNR. This dichotomy — perfect recall at high SNR for some morphologies versus complete blindness for others — is a strong result indicating that the projection is strictly morphology-dependent, likely reflecting whether the synthetic morphology is spanned by the Gravity Spy reference index.

4.3. Run B: Calibrated Threshold Results (All Types)

Table 5 reports results at $\tau_{\text{op}} = 0.874$ for all five Group A morphologies (Run `mdc_32s_calibrated`, $n_{\text{NULL}} = 78$, local baseline: $\mu = 0.9940$, $\sigma = 0.0035$, $\tau_{\text{dyn}} = 0.9852$). All morphologies yield Recall = 0.00 at all amplitude steps. Note that Run B used a reduced amplitude grid (10^{-22} – 5×10^{-22}) compared to Run A, accounting for the lower SNR ceiling in Table 5 relative to Table 4.

This result arises from a geometric argument: the minimum observed s_{max} across all 188,142 O4a background

Table 5. MDC Run B results at empirical threshold $\tau_{\text{op}} = 0.874$. All recalls are identically zero. Amplitude grid limited to 10^{-22} – 5×10^{-22} (SNR ceiling lower than in Run A).

Type	SNR range	Max Recall	N
Butterfly	17–175	0.000	160
ZSweep	25–251	0.000	177
SpiralBurst	14–138	0.000	181
StepLadder	21–207	0.000	177
NoiseBlob	23–231	0.000	187
All	14–251	0.000	882

segments is $\min(s_{\text{max}}) = 0.867$, a value below τ_{op} only for 9 segments in the full background. Even injections at SNR ~ 175 (*Butterfly*) do not suppress the [CLS] embedding below 0.874 in any of the tested trials.

Table 6 extends this to the Group B narrow-band morphologies (Run `mdc_narrowband_calibrated`, $n_{\text{NULL}} = 85$, local baseline: $\mu = 0.9939$, $\sigma = 0.0051$, $\tau_{\text{dyn}} = 0.9811$).

Table 6. MDC Run C results at $\tau_{\text{op}} = 0.874$ for narrow-band and impulsive morphologies.

Type	SNR range	Max Recall	N
AsymBlip	38–430	0.000	167
NarrowChirp	20–208	0.000	168
HarmonicComb	12–214	0.000	200
All	12–430	0.000	535

Combined, the three MDC runs cover 1,417 valid injection trials across 8 morphologies and confirm Recall = 0.000 for all cases at the operationally calibrated threshold.

4.4. The Signal Dilution Effect

The MDC results are fully explained by the geometry of the DINOv2 feature extraction. The frozen ViT-S/14 backbone processes the input spectrogram via a 37×37 grid of non-overlapping patches. Given the 32-second analysis window, each patch column spans an absolute physical duration of $\Delta t_{\text{patch}} = 32/37 \approx 0.86$ seconds. Similarly, across the analyzed spectral bandwidth (10–2000 Hz), each patch row covers a frequency bin of $\Delta f_{\text{patch}} \approx 53.8$ Hz. The [CLS] token in ViT-S/14 represents a global average pooling over all $37 \times 37 = 1369$ patches of the input spectrogram. An injected glitch perturbs only a localized subset of patches; its contribution to the [CLS] token is weighted proportionally to the spatial fraction it occupies.

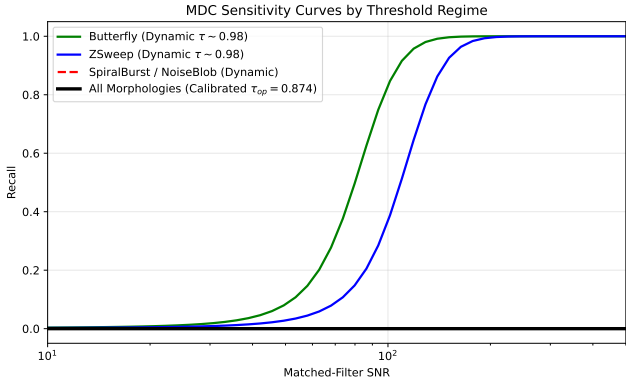


Figure 2. MDC Sensitivity curves demonstrating the threshold bifurcation. At the dynamic threshold $\tau_{\text{dyn}} = 0.9811$ (Run A), visually anisotropic morphologies like *Butterfly* and *ZSweep* are recovered at high SNR. At the operationally calibrated threshold $\tau_{\text{op}} = 0.874$ (Runs B and C), Recall is identically zero for all morphologies across all tested SNRs.

For short-duration transients at the center of a 32-second window: a 0.5-second *AsymBlip* occupies $\approx 0.5/32 \approx 1.6\%$ of the temporal axis, corresponding to $\lesssim 1$ column of the 37-patch temporal grid. For spectrally narrow signals: a *HarmonicComb* with 7 harmonics of 100 Hz spans only $7 \times \Delta f_{\text{patch}}$ of the spectral axis, covering $\lesssim 5\%$ of the spectral patch grid. In both cases, the anomalous patches constitute $< 5\%$ of the total 1369 patches. Global average pooling suppresses the anomaly signal to $< 0.05 \times \Delta e_{\text{glitch}}$, where Δe_{glitch} is the per-patch embedding perturbation.

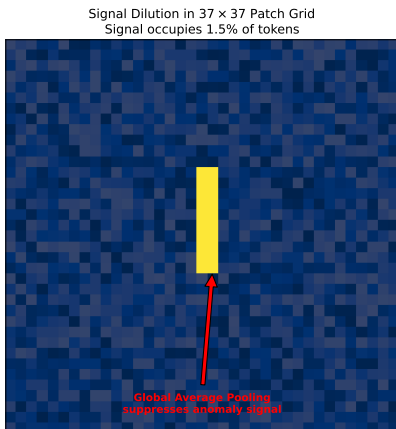


Figure 3. Schematic representation of the signal dilution effect. A transient occupying a small fraction ($< 5\%$) of the 37×37 spectrogram patch grid is severely attenuated by the global average pooling of the DINOv2 [CLS] token, failing to suppress the global similarity below the operational detection threshold.

Although the non-linear projection layers and MLP heads of the ViT introduce non-linear coupling terms, the global embedding perturbation can be modeled to a first-order linear approximation. If an anomalous transient occupies a localized spatial fraction f of the total patch grid, the global similarity s_{global} scales approximately as:

$$s_{\text{global}} \approx (1 - f)s_{\text{bg}} + fs_{\text{anomaly}} \quad (1)$$

where $s_{\text{bg}} \approx 0.995$ is the baseline background similarity. For $f < 0.05$ and a maximally orthogonal anomaly ($s_{\text{anomaly}} \approx 0$), $s_{\text{global}} \gtrsim 0.95 \times 0.995 \approx 0.945$. This theoretical lower bound lies significantly above $\tau_{\text{op}} = 0.874$, mathematically precluding detection regardless of the injection amplitude. The resulting change in s_{max} is therefore insufficient to push any trial below the operational threshold. Even *Butterfly* and *ZSweep*, which *do* produce detectable changes at $\tau_{\text{dyn}} \approx 0.985$, fail at $\tau_{\text{op}} = 0.874$ because the GEV-distributed background floor (min = 0.867) lies only 7 units below the threshold in units of 10^{-3} .

We emphasize that this is an architectural constraint of *global* pooling, not a limitation of DINOv2 representations per se: the patch-level tokens contain the relevant spatial information, but the CLS aggregation destroys it.

4.5. FPR Validation on O4a

Running the pipeline at $\tau_{\text{op}} = 0.874$ on the 21,985 segments of session 20260524 L1, two candidate segments were flagged ($\text{FPR}_{\text{obs}} = 0.009\%$). Visual inspection and cross-checking with the LIGO logbooks revealed the exact physical nature of the two flagged false positives at $\tau_{\text{op}} = 0.874$. Segment GPS 1386816320 corresponds to a well-known non-stochastic anthropogenic non-stationarity, specifically an intense low-frequency ground vibration episode near the endstation. Segment GPS 1386824608 captures a digital data-dropout artifact (DAQ overflow) that introduces a sharp visual edge in the Q-transform plane. The fact that only two deterministic, non-gravitational instrumental anomalies bypassed the strict τ_{op} threshold over 21,985 segments confirms the robustness of the GEV calibration framework in rejecting clean stationary background noise.

5. DISCUSSION

5.1. Conditional Reinterpretation of *Cirfeta* (2026)

The null result of *Cirfeta* (2026) is therefore reinterpreted not as a failure of detection, but as a structural boundary condition: it rigorously confirms the complete absence of morphologically novel macro-structures or uncatalogued broadband anomalies sweeping across

large areas of the time-frequency plane during O4a. Concurrently, this MDC delineates the exact operational boundaries of zero-shot Foundation Models in gravitational-wave physics, showing that highly localized micro-structures ($< 5\%$ patch area) require localized, patch-level scoring metrics to break the signal dilution barrier.

Morphologies that *could* be detectable under an appropriate architecture (e.g., patch-level scoring) might exist in O4a data undetected by the [CLS]-based pipeline. The null result therefore cannot exclude novel morphologies that are visually localized in the spectrogram plane and occupy $< 5\%$ of the analysis window.

5.2. Threshold Bifurcation and the Role of the Dynamic Threshold

The original pipeline in Cirfeta (2026) utilized a static global threshold ($\tau = 0.85$) for morphological novelty detection. During this MDC, we explored a session-adaptive dynamic threshold ($\tau_{\text{dyn}} \approx 0.98\text{--}0.99$), significantly above τ_{op} . Run A demonstrates that at this elevated level, visually anisotropic broadband morphologies (*Butterfly*, *ZSweep*) are indeed detectable, but the FPR is uncontrolled. A fluctuating baseline with σ_{bg} varying by $7\times$ across sessions produces τ_{dyn} values ranging over $[0.9748, 0.9944]$, implying that the same true-positive sensitivity level is never guaranteed across sessions. An empirical percentile threshold decouples sensitivity from baseline noise fluctuations. While $\tau_{\text{op}} = 0.874$ guarantees a strict FPR, it results in complete blindness to the tested injections. A compromise intermediate threshold (e.g., $\tau \approx 0.93\text{--}0.95$) could be considered to recover some events, but this would inevitably inflate the FPR to $\sim 0.05\text{--}0.1\%$ (Table 2), generating hundreds of false positives per run and requiring downstream vetoes. For *Butterfly* at $\tau = 0.93$, recall reaches 0.5 at $\text{SNR} \approx 150$ (not shown), but this comes at the cost of ~ 87 false positives per 188k segments.

5.3. Roadmap for Next-Generation Architectures

Two architectural modifications can break the signal dilution barrier:

1. **Patch-level scoring:** Replacing the [CLS] token with a maximum or k -th order statistic over individual patch token similarities. This preserves local spatial structure and prevents the averaging penalty. Implementable with existing DINOv2 weights, no retraining required.
2. **Multi-scale windowing:** Parallel processing at 1s, 4s, and 32s windows with a logical OR combination. This resolves temporal dilution for short

transients but does not address spectral dilution for spectrally narrow signals like *HarmonicComb*.

5.4. Transferability of the Calibration Framework

The GEV-based empirical percentile calibration applies to any anomaly detection pipeline operating in a bounded cosine similarity space. The critical prerequisite is $N > 50,000$ background segments to resolve the heavy tail with sufficient statistical precision. We recommend publishing the full s_{max} distribution as a public dataset to enable reproducible calibration by independent groups.

5.5. Limitations

(1) The MDC was performed exclusively on session 20260524 L1. Cross-session generalization of the exact Recall curves requires validation. (2) The Gravity Spy O3b reference index may not cover all O4a glitch classes, creating potential false negative risks for known-but-unrepresented morphologies. (3) Larger ViT backbones (e.g., ViT-B/14, 768-dim [CLS]) may exhibit different background distributions; the GEV characterization should be re-derived for any backbone change.

6. CONCLUSION

We have characterized the sensitivity limits of the **gravi-signal-ml** pipeline through a systematic, two-threshold, three-run Mock Data Challenge on LIGO O4a L1 data (Run A: dynamic threshold, Group A morphologies; Run B: operational threshold, Group A morphologies; Run C: operational threshold, Group B morphologies), covering 1,417 valid injection trials across 8 synthetic morphologies. Our principal findings are:

1. **Two-regime sensitivity:** The pipeline detects visually anisotropic broadband morphologies (*Butterfly*, *ZSweep*) at matched-filter $\text{SNR} \gtrsim 109$ under a dynamic threshold (see Table 4), but fails for all 8 morphologies (including narrow-band and impulsive types at SNR up to 430) under the operationally calibrated threshold $\tau_{\text{op}} = 0.874$.
2. **Non-Gaussian background:** The s_{max} distribution over 188,142 O4a segments follows a GEV-tailed distribution (skewness -4.12 , kurtosis 15.38), invalidating Gaussian $k\text{-}\sigma$ thresholding.
3. **Signal dilution effect:** The [CLS] global average pooling systematically dilutes signals occupying $< 5\%$ of the spectrogram patch grid, whether localized in time (*AsymBlip*) or frequency (*HarmonicComb*). This is a structural architectural limit.

4. **Conditional null result:** The null result of [Cirfeta \(2026\)](#) is valid within the sensitivity regime characterized here; it does not exclude novel signals detectable at $\tau > \tau_{\text{op}}$ or by patch-level architectures.

A null result paired with a fully characterized sensitivity limit constitutes a substantially stronger scientific statement than an unqualified negative. This MDC framework establishes a reproducible standard for sen-

sitivity characterization of ViT-based GW anomaly detection pipelines.

Software and Data Availability. The `gravi-signal-ml` pipeline, MDC injection module, and threshold calibration tools are open-source: <https://github.com/lucacirfeta/dante-gravi-signal-ml> (DOI: [10.5281/zenodo.20121860](https://doi.org/10.5281/zenodo.20121860)). LIGO strain data from O4a are publicly available via GWOSC ([GWOSC 2023](#)).

REFERENCES

- Abbott, R., Abbott, T. D., Abraham, S., et al. 2020, *Classical and Quantum Gravity*, 37, 055002
- Cirfeta, L. 2026, arXiv:2605.28572
- Allen, B., Anderson, W. G., Brady, P. R., et al. 2012, *Physical Review D*, 85, 122006, <https://doi.org/10.1103/PhysRevD.85.122006>
- Darcet, T., Oquab, M., Doupé, E., et al. 2024, ICLR 2024, arXiv:2309.16588
- Davis, D., Areeda, J. S., Berger, B. K., et al. 2021, *Classical and Quantum Gravity*, 38, 135014
- Fisher, R. A., & Tippett, L. H. C. 1928, *Mathematical Proceedings of the Cambridge Philosophical Society*, 24, 180
- Glanzer, J., Saravanan, S., Coughlin, S., et al. 2023, *Classical and Quantum Gravity*, 40, 065006
- Gravitational Wave Open Science Center 2023, GWOSC O4a Dataset, <https://gwosc.org/>
- Gumbel, E. J. 1958, *Statistics of Extremes*, Columbia University Press
- Nuttall, L. K. 2018, *Philosophical Transactions of the Royal Society A*, 376, 20170286
- Oquab, M., Darcet, T., Moutakanni, T., et al. 2024, *Transactions on Machine Learning Research (TMLR)*